VLBI USING A TELESCOPE IN EARTH ORBIT. II. BRIGHTNESS TEMPERATURES EXCEEDING THE INVERSE COMPTON LIMIT

R. P. LINFIELD, G. S. LEVY, J. S. ULVESTAD, C. D. EDWARDS, S. J. DINARDO, AND L. R. STAVERT
Jet Propulsion Laboratory, California Institute of Technology

C. H. OTTENHOFF
TRW Space and Technology Group

A. R. WHITNEY, R. J. CAPPALLO, AND A. E. E. ROGERS
Haystack Observatory

H. HIRABAYASHI, M. MORIMOTO, AND M. INOUE
Nobeyama Radio Observatory

D. L. JAUNCEY
Commonwealth Scientific and Industrial Research Organization

AND

T. NISHIMURA
Institute for Space and Astronautical Science
Received 1988 January 7; accepted 1988 June 24

ABSTRACT

VLBI observations at 2.3 GHz were conducted using an antenna of the Tracking and Data Relay Satellite System (TDRSS), in geosynchronous orbit, and two ground stations. Twenty-three of 24 sources were detected, on baselines as long as 2.15 Earth diameters. These baseline lengths gave the interferometer much better sensitivity to high brightness temperatures than any Earth-based observations. Brightness temperatures of 1–4 times the 10^{12} K inverse Compton limit were measured for 10 sources, suggesting bulk relativistic motion in these sources. Coherence values of approximately 85% for integration times of 360 s were obtained.

Subject headings: instruments — interferometry — quasars

I. INTRODUCTION

In 1986 July and August, Very Long Baseline Interferometry (VLBI) observations were performed at a frequency of 2.278 GHz, using a 4.9 m diameter orbiting antenna (*TDRSE*) of the Tracking and Data Relay Satellite System (*TDRSS*) and 64 m diameter ground stations in Australia (DSS 43) and Japan (Usuda). Those observations were successful (Levy *et al.* 1986), with fringes detected on three sources. A second experiment, in which many more (25) sources were observed, was performed in 1987 January. The observations and data correlation have been described elsewhere (Levy *et al.* 1989, hereafter Paper I; Linfield *et al.* 1987). Briefly, local oscillator (LO) phase was transferred from the TDRSS ground control station in White Sands, New Mexico, to the spacecraft. The intermediate frequency (IF) data received on the spacecraft were relayed to White Sands, where they were recorded on a Mark III data acquisition terminal (Rogers *et al.* 1983). The round-trip phase of the LO link was monitored, and the measured phases were applied as corrections to the data during correlation and fringe fitting at Haystack Observatory. This paper will present results on the coherence, data calibration, source sizes, and brightness temperatures (T_b) for the second experiment. The connection between our results and data on the same sources at other wavelengths and resolutions will be discussed by Hirabayashi *et al.* (1989, hereafter Paper III).

II. COHERENCE

The coherence of an interferometer is a measure of the phase stability of the entire system (Rogers and Moran 1981). The coherence is the ratio of the time-integrated fringe amplitude to the instantaneous fringe amplitude. Coherence losses anywhere in the system degrade the signal-to-noise ratio (S/N). In order to convert the measured correlation coefficients accurately to correlated flux densities, the magnitude of these losses must be known. At the relatively low observing frequency of 2.3 GHz, the coherence of the baseline Usuda–DSS 43 was excellent: 97% for 400 s integrations and 95% for 750 s integrations (DSS 43 was equipped with a hydrogen maser, and Usuda was equipped with a rubidium oscillator of above average phase stability). However, the coherence on the baselines to the orbiting antenna (*TDRSE*) was not as good.

In order to measure the coherence of the *TDRSE* baselines, the fringe amplitude was measured as a function of coherent integration time. This was done for all scans which had an adequate S/N and a nearly constant correlated flux density: 14 scans on the *TDRSE*–Usuda baseline and 10 scans on the *TDRSE*–DSS 43 baseline. A scan is 800 s, the time for one pass on a Mark III tape. Columns (2) and (3) of Table 1 show the measured coherence values (mean and standard deviation). For integration times less than 30 s, the standard deviations in Table 1 are dominated by the uncertainty in measuring the coherence. For integration times longer than 30 s, the standard deviations are the actual root mean square (rms) scatter in the coherence values (this scatter is substantially larger than the measurement errors). Two seconds is the shortest integration time that could be used for any scan: the coherence at 2 s has been assumed to be 1.0. Any coherence loss on time scales shorter than 2 s has been absorbed into the assumed gain/system temperature ratio of *TDRSE*. Link-phase measurements and measured differences between the White Sands

TABLE 1

TDRSE COHERENCE VALUES

Integration Time (s) (1)	Mean Coherence (2)	Coherence Standard Deviation (3)	Adjusted Mean (4)	Adjusted Standard Deviation (5)
6...............	0.986	0.007	...	...
10..............	0.982	0.007	...	...
20..............	0.975	0.010	...	...
90..............	0.926	0.054	0.937	0.035
180.............	0.873	0.131	0.909	0.042
360.............	0.777	0.184	0.857	0.066
720.............	0.486	0.282	...	...

Ground Terminal (WSGT) atomic cesium and the reference hydrogen maser frequency standards (Paper I) were applied to all the data used for the coherence measurements (as well as to all data used for later analysis).

The distribution of measured coherence values about the mean was very asymmetrical for integration times of 90–360 s. The low end of the distribution had an extended tail (comprising 7% of the total number of measured values at 90 s and 25% of the total at 360 s) which significantly affected the measured means and standard deviations for integration times of 90–360 s. However, the true effect of this tail on the determination of correlated fluxes was small. Data segments with these low coherence values could usually be identified by their anomalously low amplitude and discarded during the editing process. Therefore, the tail was deleted from the coherence distributions and the statistics were recomputed. The new means and standard deviations are shown in columns (4) and (5) of Table 1. The corrected coherence value for 360 s is 86%. For 720 s integration, the coherence distribution was very broad, with no obvious separation into a core and tail.

For integration times shorter than about 360 s, the corrections to the measured amplitudes for coherence loss have a small uncertainty ($< 7\%$). For integrations of 700–800 s (i.e., an entire Mark III tape), the coherence correction was very uncertain ($\sim 30\%$), and the resulting calibration errors were large. The integration times used for the sources in this experiment were 100, 200, 400, and 800 s. For each source, only a single integration time was used. The integration time chosen was the minimum required to achieve a S/N of 10:1 on all scans. This choice minimized calibration errors.

The coherence on *TDRSE* baselines was markedly poorer than on the Usuda–DSS 43 baseline. The most likely causes for this were imperfections in the transfer of LO phase from White Sands to *TDRSE*, uncertainties in the motion of the *TDRSE* satellite, and instabilities in the *TDRSE* electronics. Because the satellite is in Earth orbit and was not designed to do VLBI, only limited testing could be done to narrow this range of possible causes. One test involved the Doppler shift on the down-link from the spacecraft. This was measured by the link calibration (Levy *et al.* 1986; Edwards 1987; Paper I) and compared with the Doppler shift predicted from the *TDRSE* orbit ephemeris. This comparison provided a test of the accuracy of the *TDRSE* ephemeris. Ephemeris errors caused uncertainties in the change of the *TDRSE*–radio source vector which could not be calibrated with our system. The difference between the two values had a slowly varying (time scale of hours) component of about 20 mHz and a scan-to-scan scatter (time scale of ~ 15 minutes) of about 10 mHz. The long-term (hours)

velocity error was therefore on the order of 0.2 mm s^{-1}, implying an acceleration error which was too small to affect the coherence. However, the variations of ~ 0.1 mm s^{-1} on time scales of minutes could have been a significant cause of coherence loss.

The residual VLBI phase on *TDRSE* baselines (after the removal of a linear term) was plotted for the scans with the best S/N. One example is shown in Figure 1. For many of these scans, the residual phases varied in approximately a linear manner with time, except for one or two slope changes. These slope changes explain the very poor coherence at 720 s and the tail of the coherence distribution for shorter integration times. These slope changes in the phase may be due to thruster firings on the spacecraft, which are not adequately modeled by the orbit determination process.

Because the nature of the *TDRSE* coherence loss is not understood, it is not known how the coherence will vary with observing frequency. A problem in some parts of the LO link would give a coherence nearly independent of observing frequency. If imperfect orbit determination is the cause, the coherence will degrade rapidly with increasing sky frequency. The analysis of observations at 15 GHz using the same *TDRSE* satellite, which were carried out in early 1988, should provide constraints on the causes of coherence loss. For a dedicated orbiting VLBI mission, careful design of the spacecraft electronics and LO transfer system (e.g., building an optimized round-trip phase measurement capability into the system) plus improved orbit determination should provide substantially better coherence. The design goal for Quasat is 95% coherence for 300 s integrations at 22 GHz observing frequency, with the coherence known to 0.5%.

III. CALIBRATION

In order to calibrate the data from a VLBI experiment, the sensitivities (gain/system temperature) of the telescopes must be known. For most experiments involving Earth-based telescopes, the system temperature variations are monitored by periodic comparison of system noise power to the noise power of a calibration signal, injected near the horn. The strength of this calibration signal and the gain of the antenna are measured by observing sources of known flux density. This calibration method was used for the ground telescopes (Usuda and DSS 43) but could not be used for the orbiting antenna (*TDRSE*) because of the low sensitivity, and especially because of the automatic gain control on this antenna. An alternative procedure using crossing points in the *u-v* plane (Cohen *et al.* 1975) was adopted.

For sources of declination near $-12°$, the *TDRSE*–DSS 43 *u-v* track passes near the Usuda–DSS 43 track (the latter spans a much smaller region in the *u-v* plane because the equatorial component of the baseline is approximately 50 times smaller than for baselines to *TDRSE*). At that location in the *u-v* plane the correlated flux density on the two baselines must be equal. Because the two baselines involve a common telescope (DSS 43), the relative sensitivity of Usuda and *TDRSE* can be measured. In the first experiment, there was one "crossing point" on the source 1730−130: the *TDRSE*–DSS 43 track passed within 13 Mλ (out of 60 Mλ) of the Usuda–DSS 43 track in the *u-v* plane. This yielded a *TDRSE* system temperature of 320 K (assuming an aperture efficiency of 0.4; Levy *et al.* 1986), if the calibration of Usuda was correct. In the second experiment there were two "crossing points," on 1334−127 (*u-v* separation of 15 Mλ) and 0727−115 (*u-v* separation of 4 Mλ). They each
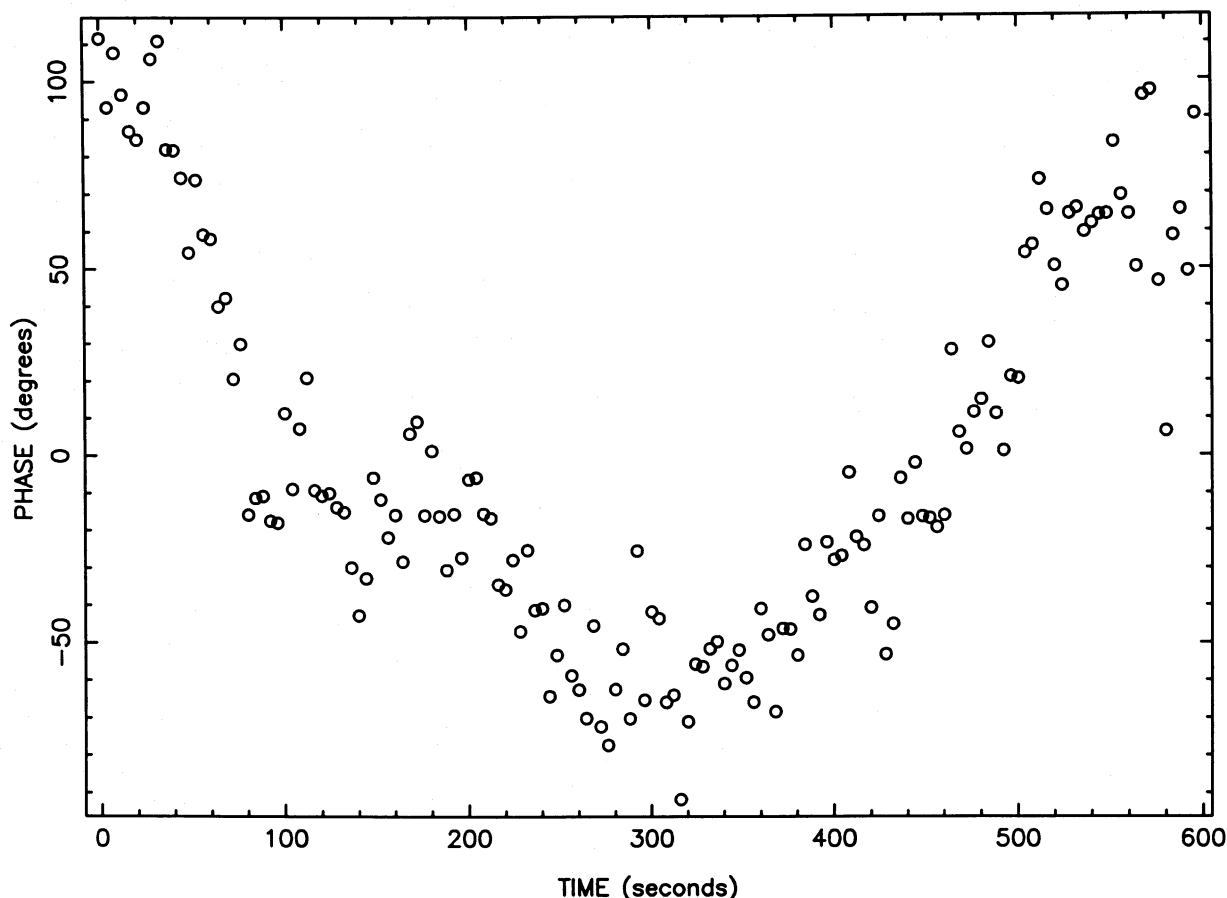
Fig. 1.—Observed phases (after corrections for the LO link and the White Sands cesium standard have been applied) for a scan on the baseline *TDRSE*–DSS 43. A linear term has been removed. The integration time for the individual points is 4 s.

yielded system temperatures for *TDRSE* (again assuming an aperture efficiency of 0.4) which agreed within 1% with the value from the first experiment. The level of this agreement is somewhat fortuitous, since it exceeds the estimated 3%–5% accuracy of the technique for our data.

Because of the small number (three) of crossing points, and the fact that no other calibration technique was available, it was necessary to assume that the gain/system temperature ratio of *TDRSE* was constant. There is some reason to expect this to be the case. Deformation of the antenna should be unimportant at the observing frequency of 2.3 GHz, and ground pickup from the Earth should add little to the system temperature except when the source is quite near ($<2°$) the limb of the Earth, as seen from *TDRSE*. *TDRSE* has an ambient temperature transistor receiver, which is thought to be fairly stable. The close agreement among the three crossing points supports the assumption of gain and system temperature stability.

There were two additional consistency checks for *TDRSE* calibration. For 3C 279 we have data of S/N $\approx$ 40 for the same Greenwich Sidereal Time (i.e., the same *u-v* point) on three days. The correlated flux densities from the three days agree to 5%. As presented in the following section, the visibility of 0727−115 varies by a factor of 5 on the *TDRSE*–Usuda baseline. This variation is accounted for nearly perfectly by a single elliptical Gaussian model. The fact that this agreement is so good suggests that the observed visibility variation is real

rather than an artifact of gain or system temperature variations.

IV. MODEL FITTING AND BRIGHTNESS TEMPERATURES

Twenty-five sources in the declination band ($-31°$, $0°$) were observed for times ranging from 13 minutes to 2 hours each. Observations of one source failed because of equipment problems at White Sands. Of the remaining 24 sources, 23 were detected on *TDRSE*–ground baselines, with baseline lengths as large as 2.15 Earth diameters ($D_\oplus$). The fringe-spacing on the longest baselines was slightly less than 1 milliarcsecond (mas). The dates of successful observation for all sources are given in Table 2. A successful observation is defined as one which yielded detectable fringes, or which we believe failed to yield fringes only because of low correlated flux from the source. The values in Table 2 are the epochs of the midpoint of observations for each day that the source was observed. The optical identifications and redshifts of the observed sources are also listed in Table 2.

Gaussian models were fitted to the visibility amplitudes of 17 of these sources. Of the remaining six sources, five were so weak that coherent integration times of 800 s were needed. The data calibration for these sources was very poor because of the large uncertainty in the coherence correction, and model fitting was therefore not performed. The sixth source had only two visibility points and one baseline, and model fitting was not done.

TABLE 2
TDRSE OVLBI OBSERVATION EPOCHS

Source Name	Epochs of Observation (UT day of 1987)	Optical Identification	Redshift[a]
0048−097	10.4, 16.4	BL Lac	...
0336−019	10.4, 16.4	QSO	0.852
0414−189	16.4	QSO	1.536
0420−014	16.5	QSO	0.915
0434−188	16.5	QSO	2.702
0454−234	16.5	QSO	[1.01]
0723−008	16.6	N galaxy	0.128
0727−115	16.6	QSO	...
0805−077	16.7	QSO	1.837
1034−293	10.7, 13.7	BL Lac	...
1124−186	13.8	QSO	1.05
1127−145	10.8, 14.8	QSO	1.187
1145−071	13.8	QSO	1.345
3C 279[b]	10.8, 13.8, 14.8	QSO	0.538
1334−127	10.8, 11.9, 14.8	QSO	0.541
1504−166	11.9	QSO	0.876
1519−273	11.9	BL Lac	...
1741−038	12.0	QSO	1.054
1921−293	11.1	QSO	0.352
1958−179	11.2	QSO	0.65
2131−021	11.2	QSO	0.557
2216−038	11.2	QSO	0.901
3C 446[c]	11.2	QSO	1.406
2345−167	11.3, 16.3	QSO	0.576

[a] The lack of an entry for a source designates an unknown redshift. The value in brackets is tentative.

[b] 3C 279 = 1253−055.

[c] 3C 446 = 2223−052.

In those cases where model fitting was performed, an adjustment in the data weights was made before fitting. For each source, all the Usuda–DSS 43 data had very nearly the same u-v values, in sharp contrast to the large spread for baselines to *TDRSE* (see Fig. 2). Model fitting with these data would have given too much weight to the value of correlated flux at the Usuda–DSS 43 u-v point, and too little weight to the variation in correlated flux across the u-v plane. To avoid this situation, only one Usuda–DSS 43 correlated flux value (an average of all measured values) was used in the fitting process. This value was given an error bar 3 times smaller than that of a typical *TDRSE*–ground amplitude (i.e., the one Usuda–DSS 43 value was given a weight equal to nine *TDRSE*–ground amplitudes). The Usuda–DSS 43 ground amplitude was weighted more heavily than a single *TDRSE*–ground amplitude for two reasons. The first is that the statistical errors on most *TDRSE*–ground amplitudes exceeded the systematic errors. The second reason is that for the single-component source models used in the fitting process, adjacent *TDRSE*–ground data sampled very similar parts of the model brightness distribution. Although the above procedure was believed to be a reasonable way of handling the data weighting, there are other possible methods. Tests showed that the resulting model parameters, and their associated errors, were quite insensitive to the details of the data-weighting scheme.

Single-component circular Gaussian models gave good fits for six of the 17 sources for which modeling was attempted. Of the other 11 sources, two had sufficiently sparse data that fitting an elliptical Gaussian was considered unwarranted. A single-component elliptical Gaussian model adequately fitted the data for eight of the remaining nine sources, with a two-component elliptical Gaussian needed for one source:

1127−145. For this source, closure phase data removed the 180° ambiguity in the model orientation. The model for this source will be discussed in Paper III. The closure phases were too noisy to constrain any of the model fluxes or shapes. Table 3 presents the source visibility and model-fitting results for the 23 sources which were detected and an upper limit for the source which was not detected. The quoted visibilities are the ratio of the correlated flux on the longest baselines to the total flux, which was measured at the two ground antennas.

The errors for the source models were derived in the following way. After the best-fitting model for each source was determined, the data errors were multiplied (by the same factor for all data on that source) so that the chi-squared agreement between model and data was 1.0 per degree of freedom. Then the size of the source model was adjusted away from the best-fit value. For each trial value of the size, the orientation (for elliptical source models) and the flux were allowed to vary so as to optimize the fit (which always gave a chi-square agreement between the model and the data larger than 1.0 because the size had been altered). However, the flux was not allowed to exceed 1.1 times the measured single-antenna flux (these measurements had a 10% uncertainty). As the size deviated from that of the best-fitting model, the chi-square difference between the model and the data increased. The errors given in Table 3 represent the range allowed at the 99% confidence level. For elliptical models, the model sizes were adjusted in three ways. The adjustments were made with one of the following three parameters held constant: major-axis size, minor-axis size, or the ratio between the two axes. The third method (fixed axial ratio) allowed the largest size variation for most sources. However, the errors in Table 3 represent the largest variations allowed in major or minor axis for any of the three methods. For circular models, only one method of adjustment, varying the radius, was performed.

The above error-estimating technique does not account for deviations from the assumption of a Gaussian source profile. If the brightness distribution were less centrally peaked than a Gaussian, the source sizes would be larger than those estimated. For the extreme (and physically unrealistic) case of a uniform brightness distribution with a sharp cutoff at the edges, the fitted Gaussian width (FWHM) would be 0.60–0.70 times the full width of the true brightness distribution. The smaller factors (near 0.60) are for less resolved sources. These factors were determined numerically by fitting Gaussian models to flat brightness distributions, and are similar to the value of 0.56 for weakly resolved sources quoted by Marscher (1983). For 0727−115 (discussed below) there are sufficient data to rule out a flat brightness distribution, but for other sources the data are inadequate to do this.

There are four sources in Table 3 (indicated with a "3" in the last column) for which the u-v coverage was nearly one-dimensional. A circular Gaussian gave a good fit to the data, but the source size perpendicular to the u-v coverage was poorly constrained. For these sources, the errors on source size were derived by adjusting the model sizes while retaining circular symmetry. The quoted errors for these sources therefore underestimate the uncertainty in source area.

The most compact source is 1519−273, with a visibility of 0.66 on a baseline of $2.02D_{\oplus}$ and a model size of 0.36 mas. This source is one of the two strongest known scintillators at 2.3 GHz in the southern hemisphere (G. Nicolson 1987, private communication); the other source is outside our declination window.

TABLE 3
Visibilities and Source Models

Source Name	Maximum Baseline ($D_\oplus$)	Total Flux (Jy)	Visibility on Maximum Baseline	Model Flux (Jy)	Major-Axis FWHM (mas)	Minor-Axis FWHM (mas)	Notes
0048−097	1.50	0.89	0.63	0.62	$0.34^{+0.33}_{-0.34}$	...	
0336−019	1.37	1.80	0.50	1.52	$0.88^{+0.35}_{-0.26}$	$0.37^{+0.37}_{-0.37}$	
0414−189	1.65	0.64	0.70	...	...	...	1
0420−014	1.38	3.64	0.63	3.43	$1.01^{+0.27}_{-0.54}$	$0.49^{+0.13}_{-0.49}$	
0434−188	1.59	0.91	0.46	...	...	...	1
0454−234	1.81	1.65	0.16	...	...	...	1
0723−008	1.31	1.89	0.16	1.07	$1.69^{+0.82}_{-1.05}$	$0.68^{+0.33}_{-0.68}$	
0727−115	1.56	3.90	0.12	3.12	$1.08^{+0.13}_{-0.12}$	$0.54^{+0.11}_{-0.15}$	
0805−077	1.18	1.15	0.45	...	...	...	2
1034−293	2.15	0.96	0.29	0.58	$0.44^{+0.12}_{-0.14}$	...	3
1124−186	1.60	0.77	0.36	...	...	...	1
1127−145	1.64	5.05	0.08	...	...	...	4
1145−071	1.35	0.85	0.26	...	...	...	1
3C 279	1.35	10.34	0.33	6.82	$2.18^{+0.16}_{-0.14}$	$0.71^{+0.05}_{-0.05}$	
1334−127	1.69	3.10	0.15	2.21	$1.22^{+0.57}_{-0.25}$	$0.52^{+0.32}_{-0.52}$	
1504−166	1.70	3.05	0.31	...	...	...	5
1519−273	2.02	1.60	0.66	1.59	$0.36^{+0.06}_{-0.06}$	...	3
1741−038	1.47	2.12	0.31	2.11	$1.26^{+0.39}_{-0.48}$	$0.87^{+0.11}_{-0.15}$	
1921−293	2.07	8.65	0.15	3.49	$0.54^{+0.06}_{-0.06}$	...	3
1958−179	1.44	1.65	0.64	1.65	$0.52^{+0.09}_{-0.27}$	...	3
2131−031	0.67	1.32	<0.20	...	...	...	
2216−038	1.23	2.61	0.51	1.78	$0.50^{+0.22}_{-0.50}$	...	
3C 446	0.94	5.20	0.09	...	...	...	5
2345−167	1.67	2.12	0.17	1.27	$1.11^{+0.29}_{-0.32}$	$0.44^{+0.47}_{-0.44}$	

NOTE.—(1) The calibration for this source was poor because of very uncertain coherence corrections. (2) The data for this source were too sparse for model fitting. (3) The u-v coverage for this source was nearly one-dimensional, and there are poor constraints on the size perpendicular to the coverage. A circular Gaussian model was used. (4) A two-component Gaussian model (see Paper III) was used for this source. (5) A circular Gaussian gave a poor fit, and the data were too sparse to justify using an elliptical Gaussian.

The sources 0727−115, 1127−145, and 3C 279 had the largest quantity of data: 2 hr, with slightly over 100 visibility points on baselines to *TDRSE* for each source. The u-v coverage for 0727−115 is shown in Figure 2, and the fit of the model to the data is shown in Figure 3. While the u-v coverage is rather unimpressive by current ground-based VLBI standards, Figure 2 shows what can be achieved with orbiting VLBI in a short period of time, even with a very small number of ground antennas and a nonoptimized orbit.

From the sources with models, the brightness temperatures can be derived (e.g., Lawrence *et al.* 1985). Model sizes are needed for this calculation—it cannot be done solely from the value of the correlated flux on the longest baseline. Table 4 lists the peak brightness temperature (in the source rest frame) for all the Gaussian models. The errors in Table 4 are derived from the model-fitting error analysis described above. The errors represent the maximum and minimum brightness temperatures for any model which agreed with the data at the 99% confidence level. Because the model fluxes and sizes are positively correlated, the errors on the brightness temperatures are in general smaller than would be suggested by the model errors in Table 3 (i.e., a larger model source size may be consistent with the data only if the model flux is substantially larger).

The values in Table 4 are all based on single-component models. For some sources (e.g., 0727−115; Fig. 3), there is good evidence that the structure is this simple, but for other

TABLE 4
Source Brightness Temperatures

Source Name	Peak Brightness Temperature[a] (10^{12} K)
0048−097	$1.25_{-0.82}(1+z)$
0336−019	$2.03_{-0.86}$
0420−014	$3.14_{-0.86}$
0723−008	$0.25^{+0.74}_{-0.10}$
0727−115	$1.28^{+0.36}_{-0.18}(1+z)$
1034−293	$0.70^{+0.61}_{-0.21}(1+z)$
3C 279	$1.59^{+0.10}_{-0.08}$
1334−127	$1.26_{-0.63}$
1519−273	$2.94^{+0.16}_{-0.61}(1+z)$
1741−038	$0.92^{+0.41}_{-0.21}$
1921−293	$3.80^{+0.76}_{-0.55}$
1958−179	$2.42^{+6.2}_{-0.51}$
2216−038	$3.20_{-1.4}$
2345−167	$0.97_{-0.38}$

[a] The errors listed correspond to the 99% confidence level. Sources for which no positive error is given have a measured size along at least one axis which is consistent with zero.
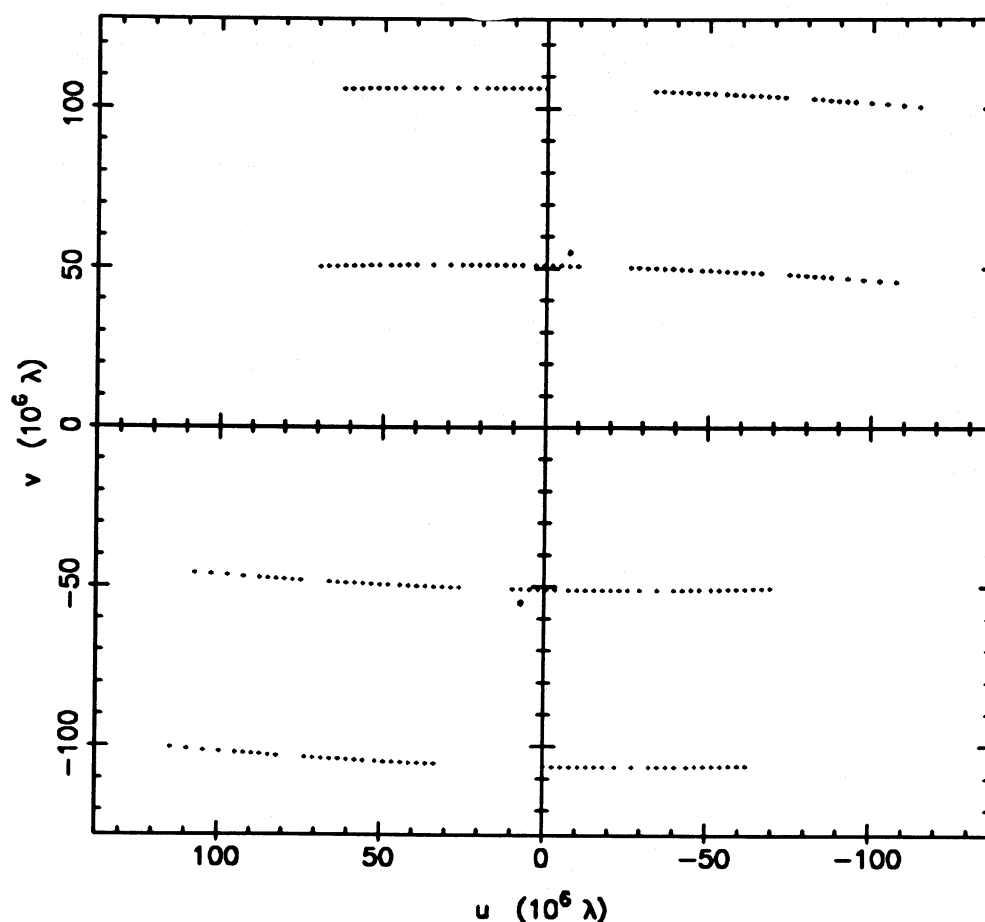
Fig. 2.—Plot showing *u-v* coverage for the source 0727−115. The tracks at $v \approx \pm 110$ Mλ are from the *TDRSE*–Usuda baseline. The tracks at $v \approx \pm 50$ Mλ are from the *TDRSE*–DSS 43 baseline. The isolated points near $v \approx \pm 60$ Mλ are from the Usuda–DSS 43 baseline.

sources the data are too sparse to rule out more complex structure. If the source brightness distribution comprises multiple components, the brightness temperature of at least one of the components will be larger than the value for a single-component model.

There are two additional uncertainties in the brightness temperature which are not listed in Table 4. The first is a possible error of up to 5%, due to uncertainty in the overall flux calibration. The second arises from the assumption of Gaussian source profiles. For the case of a uniform brightness distribution, the brightness temperatures in Table 4 should be multiplied by a factor of 0.53–0.70 (smaller factors for the sources with larger visibilities). Source profiles which are more centrally peaked than Gaussians would result in larger brightness temperatures than those given in Table 4.

In order to convert from an observed brightness temperature to the value in the source rest frame, it is necessary to multiply by $1 + z$, where z is the source redshift. This has been done in Table 4 for those sources with known redshifts.

V. DISCUSSION

The measured brightness temperatures of 10 of the 14 sources equal or exceed 10^{12} K (values below 10^{12} K are within the error bars of two of the 10). This is the first direct measurement of such large brightness temperatures for extragalactic continuum sources. The baseline lengths in this experiment were 2–3 times longer than any Earth baselines. This allowed the search for brightness temperatures exceeding 10^{12}

K in sources 4–9 times weaker than could be searched with ground arrays. Brightness temperatures of 10^{12}–10^{13} K have been inferred for a number of sources based on observed time scales for flux density variations at frequencies below 1 GHz (Condon *et al.* 1979). However, those variations may be extrinsic (Rickett, Coles, and Bourgois 1984; Heeschen *et al.* 1987), in which case the requirement for high T_b disappears.

A histogram of measured brightness temperatures is shown in Figure 4. The distribution is fairly flat out to a cutoff at $T_b \approx 4 \times 10^{12}$ K. This distribution suggests that brightness temperatures greater than 2×10^{12} K may be common among extragalactic sources. The observed cutoff may be an artifact of the experiment geometry. With baselines limited to 1.5–2 Earth diameters, it is difficult to distinguish $T_b \approx 3 \times 10^{12}$ K from larger values for sources of 1–5 Jy flux density.

For incoherent synchrotron radiation, energy losses due to inverse Compton radiation (E_{IC}) increase very rapidly with increasing T_b near 10^{12} K: $E_{IC} \propto (T_b/10^{12}$ K)^{10} (Kellermann and Pauliny-Toth 1969). This sets an upper limit to the physically allowed brightness temperature in the source rest frame. Anisotropies in the radiation field or in the electron pitch-angle distribution can alter the dependence somewhat (Jones, O'Dell, and Stein 1974). However, the very steep dependence of E_{IC} on T_b causes the maximum possible brightness temperature ($\sim 1 \times 10^{12}$ K) to be fairly insensitive to such effects (Burbidge, Jones, and O'Dell 1974). The three sources whose brightness temperatures are greater (including the errors) than 2×10^{12} K are in clear violation of the inverse Compton limit.

Although coherent emission processes produce the line emission from interstellar water masers (T_b as large as 10^{15} K; Reid and Moran 1981) and the continuum emission from pulsars, they are unlikely to be important in these extragalactic sources. A more plausible explanation for our large observed brightness temperatures is bulk relativistic motion of the emitting region toward the observer. This increases the observed T_b by the Doppler factor of the motion. The required Doppler factors ($T_b/10^{12}$ K) are consistent with those suggested by super-luminal expansion in similar sources (Unwin et al. 1983; Pearson et al. 1981).

The observations reported here comprise a survey of 24 sources for very compact structure. Visibilities on the longest baseline for each source were greater than 0.40 for 38% of the sample and greater than 0.50 for 25% of the sample. Sources with structure too compact to be resolved with ground-based VLBI are common for the flux levels studied here (>1 Jy) and are probably at least as common at lower flux levels. Future space VLBI observations, using larger antennas and more sensitive receivers, will have many sources to study.
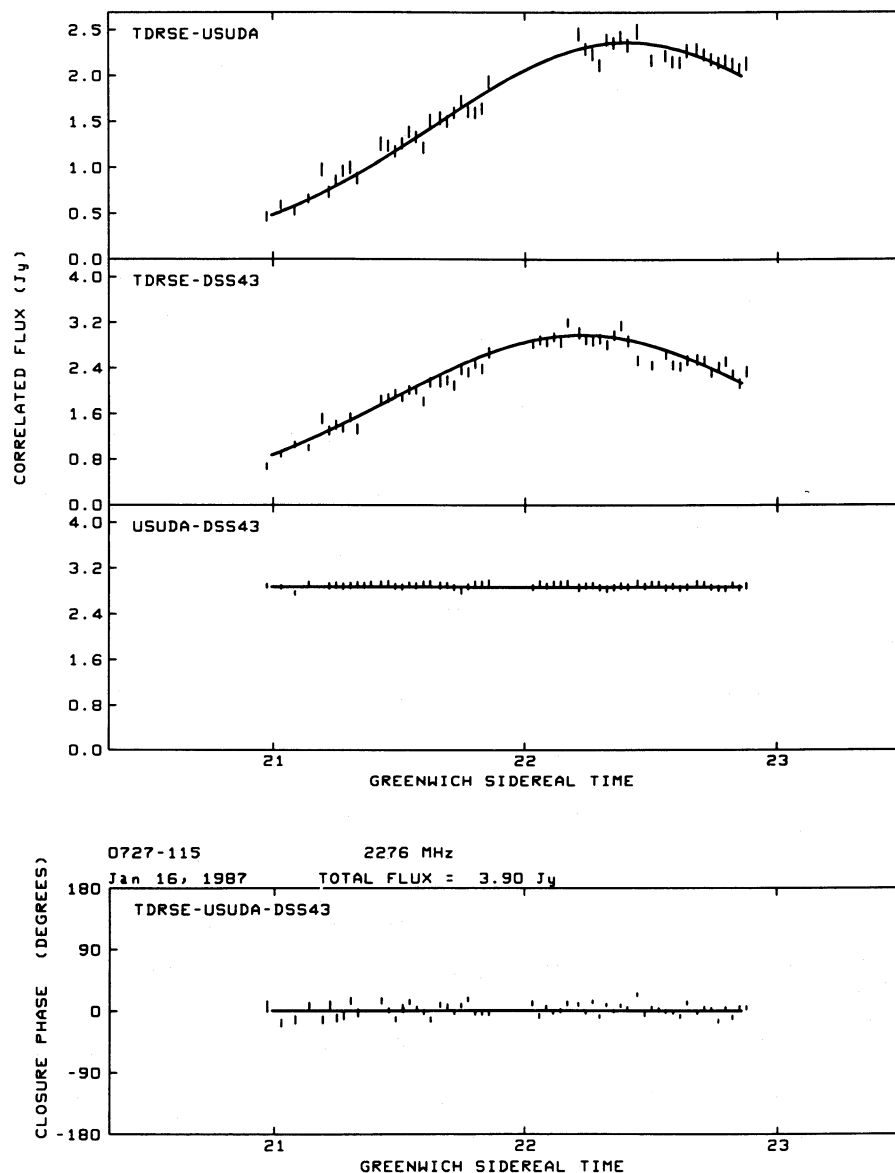
FIG. 3.—Correlated amplitudes (3 top panels) and closure phases (bottom panel) for the source 0727−115. The solid line through the data represents the visibility of the elliptical Gaussian model presented in Table 3.
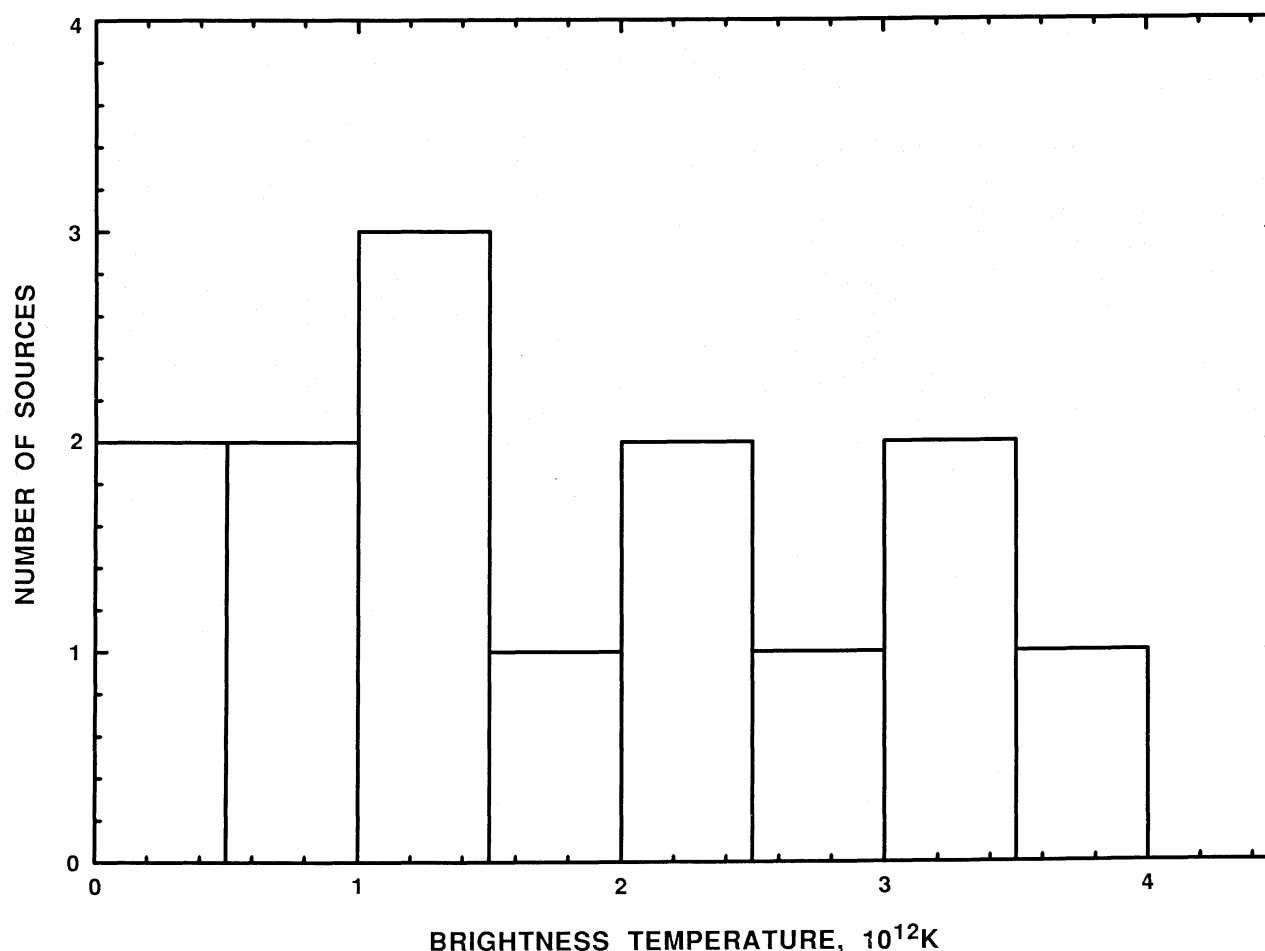
FIG. 4.—Histogram of the measured brightness temperatures for the 14 sources listed in Table 4

REFERENCES

Burbidge, G. R., Jones, T. W., and O'Dell, S. L. 1974, *Ap. J.*, **193**, 43.
Cohen, M. H., *et al.* 1975, *Ap. J.*, **201**, 249.
Condon, J. J., Ledden, J. E., O'Dell, S. L., and Dennison, B. 1979, *A.J.*, **84**, 1.
Edwards, C. D. 1987, in *Proc. Green Bank Workshop on Radio Astronomy from Space* (Green Bank: NRAO), p. 125.
Hirabayashi, H., *et al.* 1989, in preparation (Paper III).
Heeschen, D. S., Krichbaum, Th., Schalinski, C. J., and Witzel, A. 1987, *A.J.*, **94**, 1493.
Jones, T. W., O'Dell, S. L., and Stein, W. A. 1974, *Ap. J.*, **188**, 353.
Kellermann, K. I., and Pauliny-Toth, I. I. K. 1969, *Ap. J. (Letters)*, **155**, L71.
Lawrence, C. R., *et al.* 1985, *Ap. J.*, **296**, 458.
Levy, G. S., *et al.* 1986, *Science*, **234**, 187.
———. 1989, *Ap. J.*, **336**, 1098 (Paper I).

Linfield, R. P., *et al.* 1987, in *IAU Symposium 129, The Impact of VLBI on Astrophysics and Geophysics*, ed. M. J. Reid and J. M. Moran (Washington, DC: GPO), p. 457.
Marscher, A. P. 1983, *Ap. J.*, **264**, 296.
Pearson, T. J., Cohen, M. H., Linfield, R. P., Readhead, A. C. S., Seielstad, G. A., Simon, R. S., Unwin, S. C., and Walker, R. C. 1981, *Nature*, **290**, 365.
Reid, M. J., and Moran, J. M. 1981, *Ann. Rev. Astr. Ap.*, **19**, 231.
Rickett, B. J., Coles, W. A., and Bourgois, G. 1984, *Astr. Ap.*, **134**, 390.
Rogers, A. E. E., and Moran, J. M. 1981, *IEEE Trans.*, **IM-30** (No. 4), 283.
Rogers, A. E. E., *et al.* 1983, *Science*, **219**, 51.
Unwin, S. C., Cohen, M. H., Pearson, T. J., Seielstad, G. A., Simon, R. S., Linfield, R. P., and Walker, R. C. 1983, *Ap. J.*, **271**, 536.

R. J. CAPPALLO, A. E. E. ROGERS, and A. R. WHITNEY: Haystack Observatory, Westford, MA   01886

S. J. DiNARDO, C. D. EDWARDS, G. S. LEVY, R. P. LINFIELD, L. R. STAVERT, and J. S. ULVESTAD: Jet Propulsion Laboratory, 4800 Oak Grove Drive, Pasadena, CA   91109

H. HIRABAYASHI, M. INOUE, and M. MORIMOTO: Nobeyama Radio Observatory, Nobeyama 384-13, Japan

D. L. JAUNCEY: Division of Radiophysics, Commonwealth Scientific and Industrial Research Organization, Canberra, Australian Capital Territory 2601, Australia

T. NISHIMURA: Institute for Space and Astronautical Science, Tokyo 153, Japan

C. H. OTTENHOFF: TRW Space and Technology Group, Las Cruces, NM   88004